

SPECTRAL ANALYSIS OF NON-IDEAL MRI MODES: THE EFFECT OF HALL DIFFUSION

GOPAKUMAR MOHANDAS & MARTIN E. PESSAH¹

¹*Niels Bohr International Academy, Niels Bohr Institute, Blegdamsvej 17, DK-2100, Copenhagen Ø, Denmark*

ABSTRACT

The effect of magnetic field diffusion on the stability of accretion disks is a problem that has attracted considerable interest of late. In particular, the Hall effect has the potential to bring about remarkable changes in the dynamical behavior of disks that are without parallel. In this paper, we conduct a systematic examination of the linear eigenmodes in a weakly magnetized differentially rotating gas with special focus on Hall diffusion. We first develop a geometrical representation of the eigenmodes and provide a detailed quantitative description of the polarization properties of the oscillatory modes under the combined influence of the Coriolis and Hall effects. We also analyze the effects of magnetic diffusion on the structure of the unstable modes and derive analytical expressions for the kinetic and magnetic stresses and energy densities associated with the non-ideal MRI. Our analysis explicitly demonstrates that, if the dissipative effects are relatively weak, the kinetic stresses and energies make up the dominant contribution to the total stress and energy density when the equilibrium angular momentum and magnetic field vectors are anti-parallel. This is in sharp contrast to what is observed in the case of the ideal or dissipative MRI. We conduct shearing box simulations and find very good agreement with the results derived from linear analysis. As the modes in consideration are also exact solutions of the non-linear equations, the unconventional nature of the kinetic and magnetic stresses may have significant implications for the non-linear evolution in some regions of protoplanetary disks.

Keywords: magnetohydrodynamics — instabilities — accretion disks

arXiv:1702.04979v1 [astro-ph.EP] 16 Feb 2017

1. INTRODUCTION

The magnetorotational instability (MRI, Balbus & Hawley 1998), driven by differential rotation and weak magnetic fields, is considered to be the foremost mechanism of linear destabilization in astrophysical disk systems. There has been substantial ongoing interest in studying the effect of magnetic field diffusion on the MRI primarily with a view to understanding protoplanetary disk evolution (Turner et al. 2014). In particular, diffusion mediated by Hall currents has commanded a great deal of attention by virtue of its capacity to pave the way to new avenues of destabilization (Wardle 1999; Balbus & Terquem 2001). Local linear analysis has helped reveal the markedly different character of the unstable dynamics (Wardle 1999; Balbus & Terquem 2001; Wardle & Salmeron 2012) and their fundamental dependence on disk conditions, namely, the relative orientation of the net equilibrium angular momentum and magnetic field vectors and the strength of the Hall currents.

One expects to find vast swathes within a protoplanetary disk that are conducive to the prevalence of significant Hall currents as a result of ion-neutral collisions (Kunz & Balbus 2004; Pandey & Wardle 2008; Armitage 2011). This has provided great impetus in driving efforts to understand the non-linear evolution of disks influenced by non-ideal effects. A number of local shearing box simulations with Hall diffusion either in isolation or in unison with other non-ideal effects (viz. ohmic and ambipolar diffusion) have been carried out in the recent past (Sano & Stone 2002a,b; Bejarano et al. 2011; Kunz & Lesur 2013; Lesur et al. 2014; Bai 2014, 2015; Simon et al. 2015). Efforts are currently underway to perform global simulations including the Hall effect and the first among them has already been reported by Béthune et al. (2016).

While the march to conduct ever more sophisticated numerical experiments of a non-ideal MHD disk system strides onwards, certain fundamental aspects, especially those pertaining to the question of angular momentum transport may be beneficially served by a systematic examination of the non-ideal MRI eigenmodes. With this goal in mind, we revisit the local linear analysis of a uniformly magnetized disk with Hall diffusion in the shearing sheet approximation. We adopt the approach of Pessah et al. (2006); Pessah & Chan (2008) that has previously been employed to thoroughly examine the ideal and dissipative MRI eigenmodes. Here, we carry out an exhaustive analysis of the detailed eigenmode structure of the unstable and oscillatory modes affected primarily by Hall diffusion. As part of our analysis, we determine the mean kinetic and magnetic stresses and energy densities of the non-ideal MRI mode across parameter space. Our work reveals that the relative dominance of the mean Reynolds and Maxwell stresses as well as the ratio of magnetic to kinetic energy can deviate from that of ideal or dissipa-

tive MRI when the background field and angular momentum vector are anti-parallel. These departures depend intimately on the range of length scales involved and may have significant implications for the ensuing turbulence. A detailed analysis of the linear eigenmodes may also find utility in testing and benchmarking numerical algorithms designed to include Hall diffusion.

This paper is organized as follows. In Section 2, we outline the fundamental assumptions and equations involved. In Section 3, we layout the basic groundwork for our analysis and solve the eigenvalue problem. We then examine the mode properties in detail and provide a physical picture of mode behaviour in Section 4. In Section 5, we discuss the properties of the kinetic and magnetic stresses and energy densities for the unstable mode. We present the results of numerical simulations in Section 6 to test the validity of our analytical results and conclude with a summary and discussion of the potential implications in Section 7.

2. BASIC EQUATIONS AND ASSUMPTIONS

We consider a partially ionized, weakly magnetized, incompressible gas subject to ohmic, Hall and ambipolar diffusion in the presence of a gravitational field due to a central point mass. While we shall strive to retain generality wherever possible, our primary focus will nevertheless be on characterizing the effect of Hall diffusion on the linear modes.

We work in the shearing sheet (Goldreich & Lynden-Bell 1965) approximation and therefore adopt a frame of reference that co-rotates at a fiducial radius, r_0 , in the midplane of the disk. The shearing sheet frame is defined by the set of cartesian coordinates

$$x = r - r_0, \quad y = r(\phi - \Omega_0 t), \quad z = z,$$

where $x/r_0 \sim \varepsilon \ll 1$ and is based on a local expansion of the combined gravitational and centrifugal potentials to first order in ε around the fiducial radius. The angular frequency at the fiducial radius is denoted by Ω_0 and the disk is assumed to be in dominant centrifugal balance with the radial gravitational force. Consequently, all other dynamical state variables are taken to be uniform to lowest order in ε . Ignoring vertical stratification, the incompressible shearing sheet equations are given by

$$\begin{aligned} \frac{\partial \mathbf{u}}{\partial t} + (\mathbf{u} \cdot \nabla) \mathbf{u} &= 2\mathbf{u} \times \boldsymbol{\Omega}_0 + q\Omega_0^2 \nabla x^2 \\ &\quad - \frac{1}{\rho} \nabla \left(P + \frac{B^2}{8\pi} \right) + \frac{(\mathbf{B} \cdot \nabla) \mathbf{B}}{4\pi\rho} + \nu \nabla^2 \mathbf{u}, \end{aligned} \quad (1)$$

$$\frac{\partial \mathbf{B}}{\partial t} = \nabla \times (\mathbf{u}_e \times \mathbf{B}) - \frac{c}{\sigma} \nabla \times \mathbf{J}, \quad (2)$$

$$\nabla \cdot \mathbf{u} = 0, \quad (3)$$

$$\nabla \cdot \mathbf{B} = 0, \quad (4)$$

where ρ is the gas density, P is the gas pressure, \mathbf{B} is the magnetic field, σ is the constant electrical conductivity, c is the speed of light and ν is the constant fluid viscosity. The shear rate q evaluated at the fiducial radius is defined as

$$q = - \left. \frac{\partial \ln \Omega}{\partial \ln r} \right|_{r=r_0}.$$

Here, \mathbf{u} is the velocity of the neutrals and the electron velocity, \mathbf{u}_e , may be expressed as (Balbus & Terquem 2001)

$$\mathbf{u}_e = \mathbf{u} + (\mathbf{u}_e - \mathbf{u}_i) + (\mathbf{u}_i - \mathbf{u}) = \mathbf{u} - \frac{\mathbf{J}}{en_e} + \frac{\mathbf{J} \times \mathbf{B}}{\gamma_d \rho \rho_i c}, \quad (5)$$

where e is the electron charge, n_e is the electron number density, γ_d is the drag coefficient and ρ_i is the ion mass density. The current density is given by

$$\mathbf{J} = \frac{c}{4\pi} (\nabla \times \mathbf{B}). \quad (6)$$

Equations (1)–(4) admit $\mathbf{u} = -q\Omega_0 x \hat{\mathbf{y}}$ and $\mathbf{B} = B_0 \hat{\mathbf{z}}$ as a steady-state solution for the velocity and magnetic field¹. We consider Eulerian perturbations ($\delta\mathbf{u}$, $\delta\mathbf{B}$) to all the fluid variables which are assumed to depend only on the vertical coordinate and time. Rescaling the Eulerian magnetic field perturbations to have dimensions of velocity, $\delta\mathbf{b} \equiv \delta\mathbf{B}/\sqrt{4\pi\rho}$, we obtain the following set of linearized equations

$$\frac{\partial \delta u_x}{\partial t} = 2\Omega_0 \delta u_y + v_A \frac{\partial \delta b_x}{\partial z} + \nu \frac{\partial^2 \delta u_x}{\partial z^2}, \quad (7)$$

$$\frac{\partial \delta u_y}{\partial t} = (q-2)\Omega_0 \delta u_x + v_A \frac{\partial \delta b_y}{\partial z} + \nu \frac{\partial^2 \delta u_y}{\partial z^2}, \quad (8)$$

$$\begin{aligned} \frac{\partial \delta b_x}{\partial t} &= v_A \frac{\partial \delta u_x}{\partial z} + \frac{cB_0}{4\pi en_e} \frac{\partial^2 \delta b_y}{\partial z^2} \\ &+ \left(\frac{c^2}{4\pi\sigma} + \frac{B_0^2}{4\pi\rho\gamma\rho_i} \right) \frac{\partial^2 \delta b_x}{\partial z^2}, \end{aligned} \quad (9)$$

$$\begin{aligned} \frac{\partial \delta b_y}{\partial t} &= v_A \frac{\partial \delta u_y}{\partial z} - \frac{cB_0}{4\pi en_e} \frac{\partial^2 \delta b_x}{\partial z^2} - q\Omega \delta b_x \\ &+ \left(\frac{c^2}{4\pi\sigma} + \frac{B_0^2}{4\pi\rho\gamma\rho_i} \right) \frac{\partial^2 \delta b_y}{\partial z^2}. \end{aligned} \quad (10)$$

We have also defined the equilibrium Alfvén speed as

$$v_A \equiv \frac{B_0}{\sqrt{4\pi\rho_0}}. \quad (11)$$

The constraints of incompressibility, Equation (3), and solenoidality, Equation (4), require that $\delta u_z = \delta b_z = \text{const}$ and we may thus set $\delta u_z = \delta b_z = 0$ without loss of generality. Furthermore, restricting the spatial dependence of

the perturbations to the vertical dimension implies that non-linear terms vanish exactly from Equations (7)–(10). Therefore, even though we refer to the problem at hand as a linear mode analysis, the modes under consideration are expected to be long-lived (Goodman & Xu 1994).

3. EIGENVALUE PROBLEM

We conduct the linear analysis by solving the eigenvalue problem defined in the shearing sheet frame. The basic analysis in this setting has been carried out in a number of previous studies (Wardle 1999; Balbus & Terquem 2001; Kunz 2008; Wardle & Salmeron 2012). We shall however, closely inspect the characteristics of the linear eigenmodes that will enable us to establish fundamental properties of the mean kinetic and magnetic stresses and energy densities.

Assuming vertically periodic boundary conditions over the domain $[-H, H]$, where $2H$ may be taken to be the vertical extent of the disk, we express the perturbed variables as a Fourier series in z , such that

$$\delta f(z, t) = \sum_{n=-\infty}^{\infty} \hat{\delta} f(k_n, t) \exp(ik_n z), \quad (12)$$

where $k_n = n\pi/H$, with n an integer number and δf represents any of the given Eulerian perturbations². In what follows, we shall omit the subscript n for the wavenumber as well as the subscript 0 for the equilibrium variables for brevity and convenience.

The set of Equations (7)–(10), can be expressed more compactly as

$$\frac{\partial}{\partial t} \hat{\delta}(k, t) = \mathbf{L} \hat{\delta}(k, t), \quad (13)$$

where

$$\hat{\delta}(k, t) = [\delta \hat{u}_x \quad \delta \hat{u}_y \quad \delta \hat{b}_x \quad \delta \hat{b}_y]^T, \quad (14)$$

and the linear operator \mathbf{L} is

$$\mathbf{L} = \begin{bmatrix} -\omega_\nu & 2\Omega & i\omega_A & 0 \\ (q-2)\Omega & -\omega_\nu & 0 & i\omega_A \\ i\omega_A & 0 & -\omega_P & -\omega_H \\ 0 & i\omega_A & \omega_H - q\Omega & -\omega_P \end{bmatrix}, \quad (15)$$

which we have expressed entirely in terms of the frequencies defined below

$$\omega_A \equiv kv_A, \quad \text{Alfvén frequency} \quad (16)$$

$$\omega_\nu \equiv k^2\nu, \quad \text{Viscous frequency} \quad (17)$$

$$\omega_P \equiv k^2\eta_P, \quad \text{Pedersen frequency} \quad (18)$$

$$\omega_H \equiv k^2\eta_H. \quad \text{Hall frequency} \quad (19)$$

¹ Note that Equations (1)–(4) are insensitive to the presence of a uniform background toroidal field under axial symmetry.

² For weak magnetic fields, we may approximate $\Delta k = k_{n+1} - k_n \propto \beta^{-1/2}$ and thus consider the distribution of wavenumbers to be approximately continuum even for moderate values of the plasma $\beta \sim O(10^{2-3})$.

Here we have also introduced the Pedersen diffusivity

$$\eta_P = \eta_O + \eta_A \equiv \frac{c^2}{4\pi\sigma} + \frac{B^2}{4\pi\rho\gamma_d\rho_i}, \quad (20)$$

with η_O and η_A denoting the ohmic and ambipolar diffusivities respectively, as well as the Hall diffusivity

$$\eta_H \equiv \hat{\Omega} \cdot \hat{B} \frac{cB}{4\pi en_e} = s|\eta_H|. \quad (21)$$

The parameter s assumes the value of ± 1 depending on the value of the scalar product $\hat{\Omega} \cdot \hat{B}$ in Equation (21)³.

The linear operator \mathbf{L} has four eigenvalues, σ_j , and associated eigenvectors, e_j , that satisfies the eigenvalue equation

$$\mathbf{L}e_j = \sigma_j e_j \quad \text{for } j = 1, \dots, 4. \quad (22)$$

\mathbf{L} is a normal operator and therefore its eigenvectors are orthogonal if the associated eigenvalues are non-degenerate. In this case, the eigenvectors of \mathbf{L} constitute a linearly independent basis set and thus any given arbitrary vector $\hat{\delta}$ can be represented as the linear combination

$$\hat{\delta} = \sum_{j=1}^4 a_j e_j, \quad (23)$$

where a_j are in general complex valued time dependent quantities and may be thought of as the coordinates in the \mathbb{C}_4 space defined by the eigenvectors. Substituting Equation (23) in Equation (13), we obtain

$$a_j(t) = a_j(0)e^{\sigma_j t}. \quad (24)$$

Therefore

$$\hat{\delta}(k, t) = \sum_{j=1}^4 a_j(0)e^{\sigma_j t} e_j. \quad (25)$$

3.1. Dispersion relation and eigenvalues

The characteristic polynomial derived from the matrix operator \mathbf{L} , given by Equation (15) yields the dispersion relation

$$(\sigma_\nu \sigma_P + \omega_A^2)^2 - 2q\Omega^2(\sigma_P^2 + \omega_A^2) + 4\Omega^2\sigma_P^2 + (\sigma_\nu^2 + \kappa^2)\kappa_H^2 + (4-q)\Omega\omega_H\omega_A^2 = 0. \quad (26)$$

where

$$\kappa = \sqrt{2(2-q)}\Omega \quad \text{and} \quad \kappa_H = \sqrt{\omega_H(\omega_H - q\Omega)}, \quad (27)$$

are the epicyclic and the Hall-epicyclic frequency respectively. Defining κ_H makes it easier to recognize the parallel

³ With more general wavevectors and angular frequency profiles, the sign of η_H is determined by the quantity $(\mathbf{k} \cdot \boldsymbol{\omega})(\mathbf{k} \cdot \mathbf{B})$, where $\boldsymbol{\omega} = \nabla \times \mathbf{u}$ is the equilibrium vorticity (Kunz 2008).

between the Hall-Shear Instability (Rüdiger & Kitchatinov 2005; Kunz 2008) that occurs when $\kappa_H^2 < 0$ and the well-known Rayleigh instability that is present when $\kappa^2 < 0$. We also use the shorthands,

$$\sigma_\nu = \sigma + \omega_\nu \quad \text{and} \quad \sigma_P = \sigma + \omega_P. \quad (28)$$

The dispersion relation Equation (26) is rather cumbersome to solve analytically when dissipative effects are included. Nevertheless, we sketch the procedure for obtaining the roots below. We begin by converting Equation (26) to *depressed* form

$$\sigma_\alpha^4 + L\sigma_\alpha^2 + M\sigma_\alpha + N = 0, \quad (29)$$

with the coefficients

$$L = 2(\omega_A^2 - \alpha^2) + \kappa^2 + \kappa_H^2, \quad (30)$$

$$M = -2\alpha(\kappa^2 - \kappa_H^2), \quad (31)$$

$$N = (\omega_A^2 - \alpha^2)^2 + \kappa^2(\omega_A^2 + \alpha^2) - 4\omega_A^2\Omega^2 + \kappa_H^2(\kappa^2 + \alpha^2) + (4-q)\Omega\omega_H\omega_A^2, \quad (32)$$

where $\sigma_\alpha = (\sigma_\nu + \sigma_P)/2$ and $\alpha = (\omega_\nu - \omega_P)/2$.

The solutions of Equation (29) are given by

$$\sigma_\alpha = \pm_a \sqrt{-\Lambda \mp_b \sqrt{\Delta}} \pm_b \frac{M}{4\sqrt{\Delta}}, \quad (33)$$

with

$$\Lambda = \frac{3L}{4} + \frac{y}{2}, \quad \text{and} \quad \Delta = (y + L)^2 - N, \quad (34)$$

where a and b in Equation (33) mark the four possible combination of the \pm signs and y is the solution of the cubic equation

$$\left(y + \frac{L}{2}\right) [(y + L)^2 - N] = \frac{M^2}{8}. \quad (35)$$

Provided $y \neq -L/2$, we may recast Equation (35) as

$$\sqrt{(y + L)^2 - N} = \frac{M/4}{\sqrt{L/4 + y/2}}, \quad (36)$$

and substituting in Equation (33), we obtain

$$\sigma_\alpha = \pm_a \sqrt{-\left(\frac{3L}{4} + \frac{y}{2} \pm_b \frac{M/4}{\sqrt{L/4 + y/2}}\right)} \pm_b \sqrt{\frac{L}{4} + \frac{y}{2}}. \quad (37)$$

Finally, using the shorthands defined in Equation (28), we obtain the eigenvalues,

$$\sigma_j = \sigma_\alpha - \frac{\omega_\nu + \omega_P}{2} \quad \text{where } j = 1, 2, 3, 4. \quad (38)$$

Two of the solutions given by Equation (38) are oscillatory and two are exponentially varying. We derive asymptotic expressions for the eigenvalues in the dissipationless limit $\omega_\nu = \omega_P = 0$ in Appendix A.

4. THE EIGENMODES

The set of normalized eigenvectors of the operator \mathbf{L} , Equation (15), can be expressed as

$$\hat{e}_j = \frac{e_j}{|e_j|} \quad \text{for } j = 1, 2, 3, 4, \quad (39)$$

where

$$e_j = \begin{bmatrix} 2\Omega\sigma_P^2 + 2\Omega\kappa_H^2 + \omega_H\omega_A^2 \\ \sigma_P(\sigma_P\sigma_\nu + \omega_A^2) + \sigma_\nu\kappa_H^2 \\ i\omega_A(2\Omega\sigma_P - \omega_H\sigma_\nu) \\ i\omega_A(\sigma_P\sigma_\nu + \omega_A^2 - 2q\Omega^2 + 2\Omega\omega_H) \end{bmatrix}. \quad (40)$$

The eigenvector components satisfy the following relationship

$$-\frac{e_j^4}{e_j^1} = \frac{e_j^3}{e_j^2} + \frac{\omega_A q \Omega (\omega_P - \omega_\nu)}{e_j^2}, \quad (41)$$

where the superscripts denote the corresponding eigenvector component. In the absence of Hall diffusion $\omega_H \rightarrow 0$, Equation (40) reduces to Equation (48) of Pessah & Chan (2008) and to Equation (32) of Pessah et al. (2006) in the ideal limit, $\omega_\nu = \omega_P = \omega_H = 0$.

In the dissipationless limit but including Hall diffusion, multiplying Equation (40) with

$$\frac{i}{\omega_A [2\Omega(q\Omega - \omega_H) - (\sigma^2 + \omega_A^2)]}, \quad (42)$$

and using the identity (derived from the dispersion relation)

$$\frac{2\Omega\sigma_j^2 + 2\Omega\kappa_H^2 + \omega_H\omega_A^2}{2\Omega(q\Omega - \omega_H) - (\sigma_j^2 + \omega_A^2)} = \frac{\sigma_j^2 + \omega_A^2 + \kappa_H^2}{2\Omega - \omega_H}, \quad (43)$$

we may recast Equation (40) in the more useful form

$$\hat{e}_j = \begin{bmatrix} iF/\omega_A & i\sigma_j F/\omega_A G & -\sigma_j/G & 1 \end{bmatrix}^T, \quad (44)$$

where

$$F = (\sigma_j^2 + \omega_A^2 + \kappa_H^2)(2\Omega - \omega_H)^{-1}, \quad (45)$$

$$G = [2\Omega(q\Omega - \omega_H) - (\sigma_j^2 + \omega_A^2)](2\Omega - \omega_H)^{-1}. \quad (46)$$

The physically meaningful perturbation components are then obtained from the real part of the eigenvector as

$$\delta_j(z, t) = \Re[\hat{\delta}(k, t) \exp(ikz)]. \quad (47)$$

Since δ_j is a function of the real spatial variable z and time t , we can draw geometrical meaning from the eigenvector, Equation (47), and construct a physical picture of the mode evolution.

A defining property is the relative orientation of the velocity and magnetic field components associated with the perturbations by taking the scalar product of the two dimensional vectors defined by $\delta_u = [e_j^1 \ e_j^2]$ and $\delta_b = [e_j^3 \ e_j^4]$, i.e., $\delta_u \cdot \delta_b = u_0 b_0 \cos \theta_j$, where

$$u_0 = \sqrt{|e_j^1|^2 + |e_j^2|^2} \quad \text{and} \quad b_0 = \sqrt{|e_j^3|^2 + |e_j^4|^2} \quad (48)$$

In what follows, it shall be expedient, on occasion, to use the dimensionless variables

$$\tilde{k} = \frac{k v_A}{\Omega}, \quad \tilde{\eta}_H = \frac{\eta_H \Omega}{v_A^2}, \quad \tilde{\eta}_P = \frac{\eta_P \Omega}{v_A^2}. \quad (49)$$

4.1. The Oscillatory Eigenmode

The Hall effect is distinct from the other kinds of magnetic diffusion in that the electromotive forces it induces act as a ‘‘magnetic-Coriolis’’ force (Balbus & Terquem 2001). This property leads to the polarization of the oscillatory eigenmodes in a manner akin to that rendered by the kinetic Coriolis force. The only effect that ohmic and ambipolar diffusion has on these modes is to damp the wave amplitude over time. Since the effect of dissipation on the eigenmodes has been studied extensively in Pessah & Chan (2008), we shall focus exclusively on the geometric aspects of the oscillatory modes due to Hall diffusion alone and set $\omega_\nu = \omega_P = 0$ here.

In order to provide a geometrical representation of the modes in physical space, it is useful to first consider the norm of the ratios

$$\left| \frac{e_j^2}{e_j^1} \right|^2 = \left| \frac{e_j^3}{e_j^4} \right|^2 = \frac{|\sigma_j|^2 (2\Omega - \omega_H)^2}{[2\Omega(q\Omega - \omega_H) - (\sigma_j^2 + \omega_A^2)]^2}. \quad (50)$$

Note that we retain the label j to denote the eigenmode here as the unstable modes may also become oscillatory beyond a cut-off wavenumber for certain values of the Hall parameter. Using the dispersion relation, Equation (26), the ratio defined in Equation (50) becomes

$$\left| \frac{e_j^2}{e_j^1} \right|^2 = \left| \frac{e_j^3}{e_j^4} \right|^2 = -\frac{|\sigma_j|^2 \sigma_j^{-2}}{1 + \mu}, \quad (51)$$

where we have defined the quantity

$$\mu \equiv q\Omega \frac{[\sigma_j^2 + \omega_A^2 + 2\Omega(\omega_H - q\Omega)]}{\sigma_j^2(2\Omega - \omega_H)}. \quad (52)$$

When the mode is purely oscillatory, $-|\sigma_j|^2 \sigma_j^{-2} = 1$ and Equation (51) simply describes an ellipse with the components of δ_u and δ_b representing the semi-major and minor axes. The eccentricity of the ellipse, ϵ , is related to μ as

$$\epsilon^2 = \begin{cases} |\mu| & \text{if } \mu < 0, \\ \mu/(1 + \mu) & \text{if } \mu > 0. \end{cases} \quad (53)$$

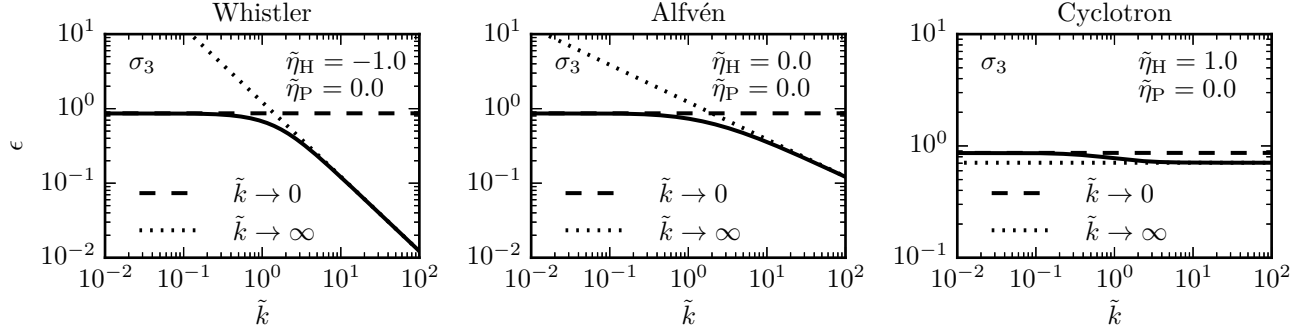


Figure 1. The eccentricity ϵ of the polarized oscillatory mode, $\sigma_3 = i\omega$, as a function of wavenumber for $q = 1.5$ and $\tilde{\eta}_H = -1.0, 0.0, 1.0$. Asymptotic approximations in the low wavenumber limit ($\tilde{k} \rightarrow 0$) and the high wavenumber limit ($\tilde{k} \rightarrow \infty$) are represented by the dashed and dotted lines respectively. The left panel corresponds to a Whistler mode, the central panel corresponds to an Alfvén mode and the right panel corresponds to a cyclotron mode; all three subject to the combined influence of rotation and shear (see Appendix A).

With the aid of the asymptotic forms for the eigenvalues, Equations (A7)–(A8), we can determine the asymptotic behaviour of the eccentricity as given below

$$-2 < \tilde{\eta}_H \leq -1/2 :$$

$$\sigma_3 : \lim_{k \rightarrow 0} \epsilon^2 \sim \frac{q}{2}, \quad \lim_{k \rightarrow \infty} \epsilon^2 \sim \frac{q\Omega}{|\omega_H|}, \quad (54)$$

$$-1/2 < \tilde{\eta}_H < 0 :$$

$$\sigma_1 : \quad \lim_{k \rightarrow \infty} \epsilon^2 \sim \frac{q\Omega|\omega_H|}{\omega_A^2 + 2\Omega|\omega_H|},$$

$$\sigma_3 : \lim_{k \rightarrow 0} \epsilon^2 \sim \frac{q}{2}, \quad \lim_{k \rightarrow \infty} \epsilon^2 \sim \frac{q\Omega}{|\omega_H|}, \quad (55)$$

$$\tilde{\eta}_H = 0 :$$

$$\sigma_1 : \quad \lim_{k \rightarrow \infty} \epsilon^2 \sim \frac{q\Omega}{\omega_A},$$

$$\sigma_3 : \lim_{k \rightarrow 0} \epsilon^2 \sim \frac{q}{2}, \quad \lim_{k \rightarrow \infty} \epsilon^2 \sim \frac{q\Omega}{\omega_A}, \quad (56)$$

$$\tilde{\eta}_H > 0 :$$

$$\sigma_1 : \quad \lim_{k \rightarrow \infty} \epsilon^2 \sim \frac{q\Omega}{\omega_H},$$

$$\sigma_3 : \lim_{k \rightarrow 0} \epsilon^2 \sim \frac{q}{2}, \quad \lim_{k \rightarrow \infty} \epsilon^2 \sim \frac{q\Omega|\omega_H|}{\omega_A^2 + 2\Omega\omega_H}. \quad (57)$$

The eccentricity of the Alfvén and Whistler modes (see Appendix A for mode nomenclature) decreases with increasing wavenumber and the polarization becomes increasingly circular. The eccentricity is generally maximum in the limit $k \rightarrow 0$, and has the value $\epsilon_{\max} = \sqrt{q/2}$, which incidentally shares the value of the Oort constant for a differentially rotating disk. The eccentricity of the cyclotron mode (see Appendix A) is only marginally lower than the maximum ϵ_{\max} at large wavenumbers as its frequency is bounded at ω_G , see Appendix A. In Figure 1, we show the three distinct ways in

which the eccentricity of the oscillatory mode can vary as a function of the wavenumber with the asymptotic forms derived above to match.

Using Equations (41) and (51), the relative orientation of $\delta_{\mathbf{u}}$ and $\delta_{\mathbf{b}}$ for the oscillatory modes can be described by the angle

$$\cos \theta_\omega = -\sqrt{\frac{1 - \epsilon^2(k)}{[1 - \epsilon^2(k) \cos^2 \varphi][1 - \epsilon^2(k) \sin^2 \varphi]}}, \quad (58)$$

where $\varphi = kz + \omega t$. In general, θ_ω oscillates in time, so $\delta_{\mathbf{u}}$ and $\delta_{\mathbf{b}}$ move in and out of phase as φ changes by a factor of $\pi/2$.

Figure 2 charts the evolution of the net velocity vector of the positive branch eigensolutions, σ_1 and σ_3 , over a half-period for a fixed wavenumber and two different values of the Hall parameter. Notice that the polarization of σ_1 for $\tilde{\eta}_H = 1$ as well as σ_3 for $\tilde{\eta}_H = -1.5$ is very nearly circular whereas the polarization of σ_3 for $\tilde{\eta}_H = 1$ is visibly elliptical. We also remind the reader that any determination of the direction of polarization (right or left) is to be made by examining the eigenvector, Equation (47). For instance, σ_1 associated with $\tilde{\eta}_H = 1$ is right elliptically polarized whereas σ_3 associated with $\tilde{\eta}_H = -1.5$ is left elliptically polarized even though both behave like a Whistler mode at large wavenumbers.

4.2. The Non-Ideal MRI Eigenmode

Here, we examine the properties of the eigenvector corresponding to the non-ideal MRI mode. Closed form expressions are much easily derived in the absence of viscous effects and so we shall set $\omega_\nu = 0$ hereafter. This would correspond to considering the very low magnetic Prandtl number limit $\text{Pm} \equiv \nu/\eta_P \rightarrow 0$, which is also the relevant regime of parameter space with regard to protoplanetary disks.

We express below the main characteristic scales associated with the unstable mode obtained from the dispersion relation, Equation (26) in the inviscid limit (Wardle & Salmeron

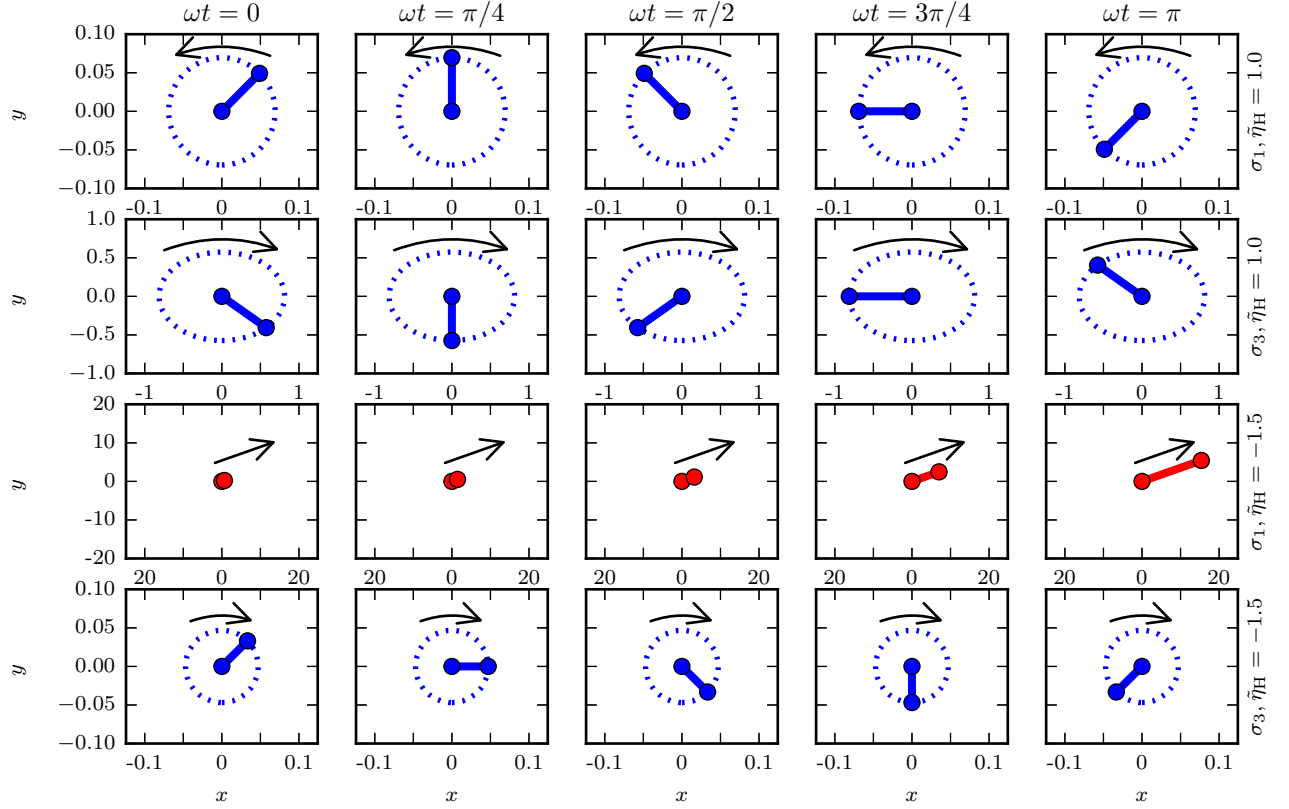


Figure 2. Visualization of the eigenmodes σ_1 and σ_3 in the horizontal plane at $kz = \pi/4$ for $\tilde{k} = 10$, $q = 1.5$ and two different values of the Hall diffusivity, $\tilde{\eta}_H = 1.0, -1.5$. The thick solid line denotes the velocity vector and the arrows indicate the direction of polarization (right or left, See Appendix A) of the corresponding eigenmodes as seen by an observer looking down at the midplane from above. Each row of plots depicts the mode evolution over one half period in time.

2012) and applicable in the parameter space defined by $(\tilde{\eta}_H, \tilde{\eta}_P)$.

The critical wavenumber beyond which the non-ideal MRI is cut-off is

$$\tilde{k}_c^2 = \frac{2q[1 + (2-q)\tilde{\eta}_H]}{1 + (4-q)\tilde{\eta}_H + 2(2-q)(\tilde{\eta}_H^2 + \tilde{\eta}_P^2)}. \quad (59)$$

A suitable combination of the Pedersen and Hall diffusivities can lead to $\tilde{k}_c \rightarrow \infty$. This occurs when the denominator in Equation (59) vanishes

$$1 + (4-q)\tilde{\eta}_H + 2(2-q)(\tilde{\eta}_H^2 + \tilde{\eta}_P^2) = 0. \quad (60)$$

The wavenumber at which the growth rate is maximum is

$$\tilde{k}_m^2 = \frac{-2\gamma_m^2[\gamma_m^2 + 2(2-q)]}{2\gamma_m^2 - 2q - [\gamma_m^2 + 2(2-q)](q\tilde{\eta}_H - 2\gamma_m\tilde{\eta}_P)}, \quad (61)$$

and the maximum growth rate γ_m normalized by Ω satisfies

$$\tilde{\eta}_H = \frac{16q\tilde{\eta}_P\gamma_m}{4q^2 - 16\gamma_m^2} - \frac{2}{\gamma_m^2 + 2(2-q)}. \quad (62)$$

In a portion of the parameter space defined by $(\tilde{\eta}_H, \tilde{\eta}_P)$, the maximum growth rate is reached asymptotically as the

wavenumber approaches infinity and the denominator of Equation (61) vanishes. The growth rate in this region is obtained by solving

$$[\gamma_m^2 + 2(2-q)](\tilde{\eta}_H^2 + \tilde{\eta}_P^2) + [2\tilde{\eta}_P\gamma_m + (4-q)\tilde{\eta}_H] + 1 = 0. \quad (63)$$

This regime will be the subject of greater discussion in the following section.

Let us now examine how the planes containing the velocity and magnetic vectors δ_u and δ_b associated with the unstable mode are oriented relative to each other. Using Equation (41), we find

$$\cos \theta_\gamma \equiv \frac{e_\gamma^1 e_\gamma^3 + e_\gamma^2 e_\gamma^4}{b_0 u_0} = -\frac{\omega_\Lambda \omega_P q \Omega e_\gamma^1}{b_0 u_0}. \quad (64)$$

In the absence of dissipation, $\omega_P \rightarrow 0$, $\theta_\gamma = \pi/2, 3\pi/2$, and δ_u and δ_b are orthogonal to each other. Additionally, the angle ψ subtended by the velocity vector δ_u with respect to the x axis in the xy plane is simply given by $\tan \psi = |e_\gamma^2|/|e_\gamma^1|$.

Figure 3 illustrates δ_u and δ_b projected on to the mid-plane of the disk for four representative values of the Hall diffusiv-

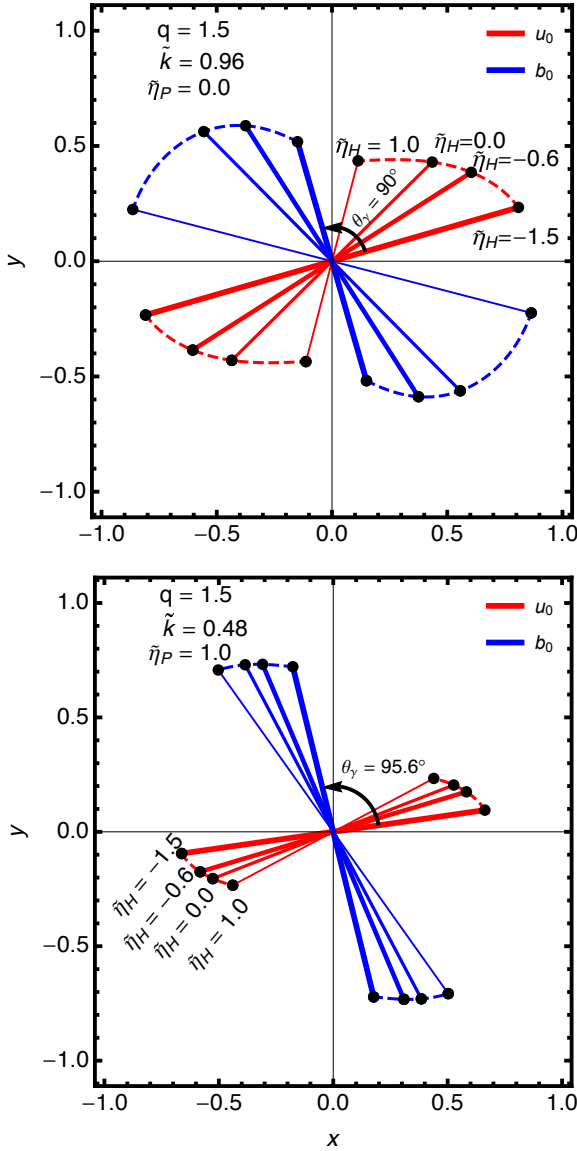


Figure 3. A geometrical representation of the velocity field δ_b and the magnetic field δ_b projected on the horizontal plane of the disk for different values of the Hall parameter, $\tilde{\eta}_H = -1.5, -0.6, 0.0, 1.0$. The top panel presents the case without dissipation $\tilde{\eta}_P = 0$ evaluated at $\tilde{k} = 0.96$ and the bottom panel illustrates the case with magnetic dissipation $\tilde{\eta}_P = 1.0$ evaluated at the wavenumber $\tilde{k} = 0.48$. A general trend that one observes is for the velocity vector to lean in towards the positive x axis and for the magnetic vector to lean in towards the positive y axis with increasingly negative Hall parameter. The magnetic and velocity vector are however only orthogonal to each other in the dissipationless limit and when $\text{Pm} = 0$.

ity $\tilde{\eta}_H$, for a fixed wavenumber \tilde{k} , with and without dissipation ω_P . The angle ψ becomes smaller with increasingly negative values of the Hall parameter, $\tilde{\eta}_H$. This is shown graphically in Figure 4 for the wavenumber \tilde{k}_m at which the growth rate of the ideal MRI is maximum. One can also see

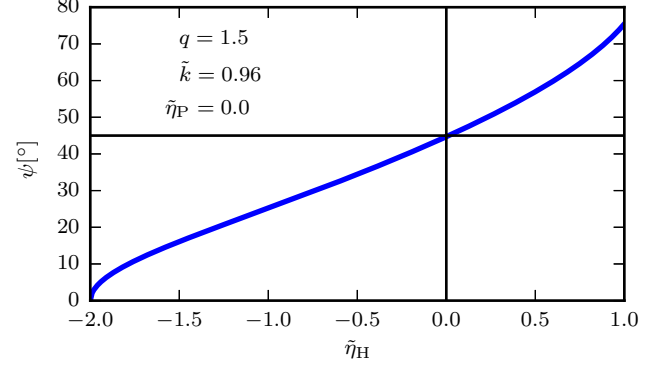


Figure 4. The angle ψ between the velocity vector δ_u and the x axis plotted as a function of the Hall parameter $\tilde{\eta}_H$. The angle is calculated from the eigenvector components evaluated at the wavenumber, \tilde{k}_m for the ideal MRI.

that the velocity and magnetic vectors are not quite orthogonal when $\omega_P \neq 0$ (Pessah & Chan 2008).

Finally, the ratio of the magnitudes of the magnetic vector to the velocity vector, b_0/u_0 , can also be computed from the eigenvector components Equation (40). Figure 5 measures this ratio as a function of wavenumber for different values of the Hall parameter. We find that this ratio becomes lesser than unity implying that the magnetic perturbation is weaker in comparison to the velocity perturbation when $\tilde{\eta}_H < 0$ and for a very large range of wavenumbers with $\tilde{\eta}_P < 1$. This feature will be of particular interest with regard to the transport stresses of the non-ideal MRI unstable mode and will be explored further in the following section.

5. KINETIC AND MAGNETIC STRESSES AND ENERGY DENSITIES

We now use the results of the eigenmode analysis to ascertain the properties of the mean kinetic and magnetic stresses and energy densities. In particular, we focus on the xy component of the Reynolds and Maxwell stresses of the MRI mode. We define the mean Reynolds and Maxwell stresses as

$$R_{ij}(t) = \overline{\delta u_i(z, t) \delta u_j(z, t)} \quad \text{and} \quad M_{ij}(t) = \overline{\delta b_i(z, t) \delta b_j(z, t)}, \quad (65)$$

where the over-line denotes the vertical average over the domain $[-H, H]$. In terms of their Fourier components, the stress components are given by (see Pessah et al. 2006 for

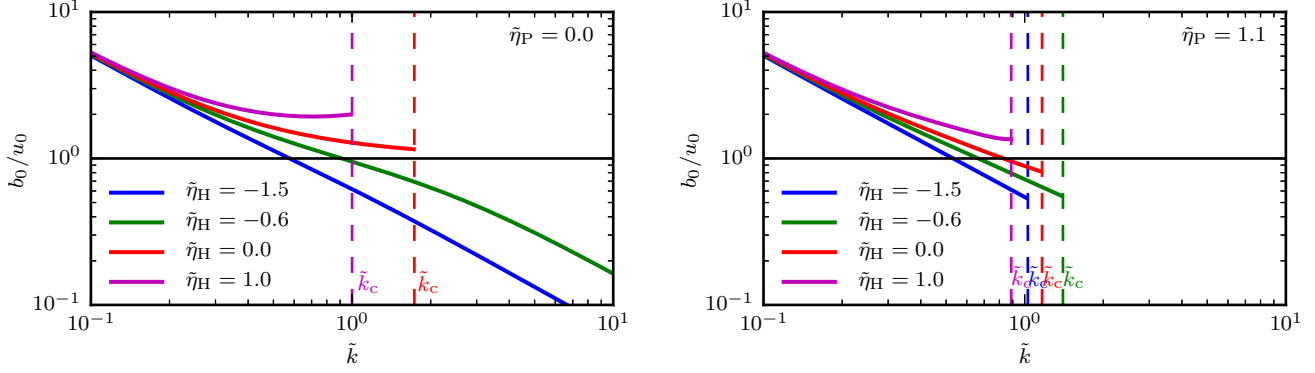


Figure 5. The ratio b_0/u_0 of the MRI unstable eigenmode for different values of the Hall parameter $\tilde{\eta}_H$ without dissipation (left) and with dissipation (right). This ratio becomes lesser than unity for $\tilde{\eta}_H < 0$ and it has implications for the relative strengths of the magnetic and kinetic stresses pertinent to angular momentum transport.

the derivation)⁴

$$R_{ij}(t) \equiv 2 \sum_{n=1}^{\infty} \Re[\delta \hat{u}_i(k_n, t) \delta \hat{u}_j^*(k_n, t)], \quad (66)$$

$$M_{ij}(t) \equiv 2 \sum_{n=1}^{\infty} \Re[\delta \hat{b}_i(k_n, t) \delta \hat{b}_j^*(k_n, t)]. \quad (67)$$

The xy component of the Reynolds and Maxwell stress tensor associated with the Hall-MRI unstable eigenmode are

$$R_{xy}(t) = 2 \sum_{n=1}^{\infty} \mathcal{R}_{xy}(k_n) e^{2\sigma(k_n)t}, \quad (68)$$

$$\mathcal{M}_{xy}(t) = 2 \sum_{n=1}^{\infty} \mathcal{M}_{xy}(k_n) e^{2\sigma(k_n)t}, \quad (69)$$

where

$$\mathcal{R}_{xy}(k_n) = \frac{\Re[e_\gamma^1 e_\gamma^{2*}]}{\|e_\gamma\|^2}, \quad (70)$$

$$\mathcal{M}_{xy}(k_n) = \frac{\Re[e_\gamma^3 e_\gamma^{4*}]}{\|e_\gamma\|^2}. \quad (71)$$

The trace of the tensors R_{ij} and M_{ij} gives us the mean kinetic and magnetic energy densities respectively

$$E_K(t) = 2 \sum_{n=1}^{\infty} \mathcal{E}_K(k_n) e^{2\sigma(k_n)t}, \quad (72)$$

$$E_M(t) = 2 \sum_{n=1}^{\infty} \mathcal{E}_M(k_n) e^{2\sigma(k_n)t}, \quad (73)$$

where

$$\mathcal{E}_K(k_n) = \frac{\mathcal{R}_{xx}(k_n) + \mathcal{R}_{yy}(k_n)}{2}, \quad (74)$$

$$\mathcal{E}_M(k_n) = \frac{\mathcal{M}_{xx}(k_n) + \mathcal{M}_{yy}(k_n)}{2}. \quad (75)$$

⁴ In order to keep track of the various modes contributing to the mean values, we restore the wavenumber index n throughout this section.

The quantities \mathcal{R}_{xy} , \mathcal{M}_{xy} , \mathcal{E}_K and \mathcal{E}_M represent the contribution of each mode k to the mean values of the corresponding functions (Pessah et al. 2006).

The ratio of the xy components of Maxwell stress to the Reynolds stress is a non-trivial function of k_n . In the ideal limit (with $\omega_\nu = \omega_P = \omega_H = 0$), using the dispersion relation, one can easily see that $\mathcal{M}_{xy} > \mathcal{R}_{xy}$ for the full range of unstable modes, k_n . In the dissipationless limit, where $\omega_\nu = \omega_P = 0$ but $\omega_H \neq 0$, this ratio reduces to

$$\frac{-\mathcal{M}_{xy}(k_n)}{\mathcal{R}_{xy}(k_n)} = \frac{\omega_A^2 (2\Omega - \omega_H)^2}{[\gamma^2(k_n) + \omega_A^2 + \kappa_H^2]^2}. \quad (76)$$

Interestingly, the ratio defined in Equation (76) is only greater than unity if

$$\tilde{k}_n^2 < \tilde{k}_i^2 = \frac{(q-2)}{\tilde{\eta}_H}. \quad (77)$$

The wavenumber \tilde{k}_i is purely imaginary if $\tilde{\eta}_H > 0$ and infinite valued if $\tilde{\eta}_H = 0$. However, when $\tilde{\eta}_H < 0$ and $q < 2$, \tilde{k}_i is finite and real valued. This implies that there is a range of unstable wavenumbers for which $\mathcal{R}_{xy} > \mathcal{M}_{xy}$. It is rather difficult to derive an equivalent expression for \tilde{k}_i in closed form with $\omega_P \neq 0$ since this would require solving a quartic equation in both \tilde{k} and γ . However, numerical calculations hint at the presence of such a scale with dissipative effects present as well and we comment further on this in the following section. As we shall discuss below, the potential for a role-reversal of the dominant stress components are directly tied to the exact nature of the unstable mode in different parts of parameter space.

The characteristic variables that specify the wavenumber at which the growth rate is quenched \tilde{k}_c , and the wavenumber at which the growth rate is maximum \tilde{k}_m , divides the parameter space defined by $(\tilde{\eta}_H, \tilde{\eta}_P)$ into three regions I, II and III as described in Wardle & Salmeron (2012). Region I is defined by the space outside of a semi-circle in the coordinates $(\tilde{\eta}_H, \tilde{\eta}_P)$ spanning from $(-1/2, 0)$ to $(-2, 0)$. Here

the unstable mode has a finite \tilde{k}_c and \tilde{k}_m . The space contained within the aforementioned semi-circular locus and an arc extending from $(\tilde{\eta}_H, \tilde{\eta}_P) = (-4/5, 0)$ to $(-2, 0)$ is designated Region II. Here the unstable mode has a finite \tilde{k}_m but \tilde{k}_c is infinite. Finally, the area enclosing the lower boundary of Region II and the horizontal axis $\tilde{\eta}_H$ is designated Region III. In this region, both \tilde{k}_c and \tilde{k}_m are infinite. The region $\tilde{\eta}_H < -2$ is stable to the MRI for all values of $\tilde{\eta}_P$. This classification will be useful in specifying the dominant stresses in parameter space as we discuss below.

5.1. Stresses and Energies in Region I

As mentioned above, the MRI growth is cut-off at a finite wavenumber in Region I. This implies that the major contributions to Equations (68), (69), (72) and (73) come from a finite range of unstable wavenumbers $n = 1$ to $n = N_c$ where N_c labels the cut-off wavenumber \tilde{k}_c . At late times, the mean stresses and energy densities may then be expressed as

$$R_{xy}(t) = 2 \sum_{n=0}^{N_c} \mathcal{R}_{xy}(k_n) e^{2\gamma(k_n)t} + \dots, \quad (78)$$

$$M_{xy}(t) = 2 \sum_{n=0}^{N_c} \mathcal{M}_{xy}(k_n) e^{2\gamma(k_n)t} + \dots, \quad (79)$$

$$E_K(t) = 2 \sum_{n=0}^{N_c} \mathcal{E}_K(k_n) e^{2\gamma(k_n)t} + \dots, \quad (80)$$

$$E_M(t) = 2 \sum_{n=0}^{N_c} \mathcal{E}_M(k_n) e^{2\gamma(k_n)t} + \dots, \quad (81)$$

with the dots representing oscillatory contributions that we may safely neglect. Within this region of parameter space, it is reasonable to expect that at late times during the linear evolution, the kinetic and magnetic stresses are dominated by contributions linked to the scale \tilde{k}_m . In the dissipationless limit, we can thus expect

$$\lim_{t\Omega \gg 1} \frac{-M_{xy}}{R_{xy}} \sim \frac{-\mathcal{M}_{xy}}{\mathcal{R}_{xy}} \Big|_{\tilde{k}_m} = \frac{(4-q)[(4-q)\tilde{\eta}_H + 2]}{2q}. \quad (82)$$

Equation (82) trivially reduces to Equation (65) of Pessah et al. (2006) in the ideal MHD limit. Deriving an equivalent analytical expression for the late time stress ratios in the presence of dissipation is tedious but can easily be computed numerically. However, numerical calculations also reveal that a real valued \tilde{k}_i may be present for certain values of $\tilde{\eta}_P$ in Region I and the scales are arranged in the order $\tilde{k}_m < \tilde{k}_i \lesssim \tilde{k}_c$. Nevertheless, the ratio of the stress components will be dominated by the fastest growing mode, at which one always finds $-\mathcal{M}_{xy} > \mathcal{R}_{xy}$. In the dissipationless limit, \tilde{k}_i is never real valued in Region I.

5.2. Stresses and Energies in Regions II and III

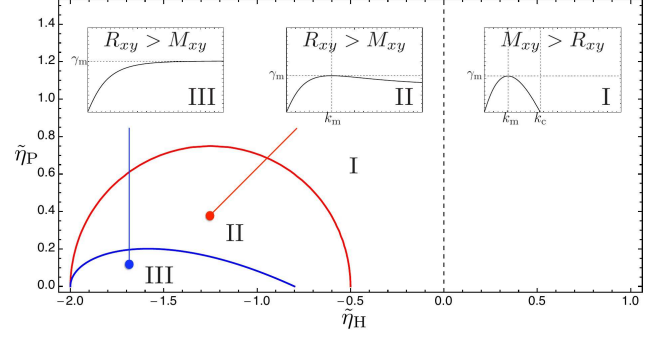


Figure 6. The parameter space defined by $\tilde{\eta}_H$ and $\tilde{\eta}_P$ demarcated into three regions I, II and III based on the distinct characteristic traits of the MRI for the said range of parameter values. The figure is identical to Fig 5 of Wardle & Salmeron (2012) with the relative strengths of the xy kinetic and magnetic stress components additionally specified.

The unstable mode grows at a uniform rate for a wide range of wavenumbers that extend infinitely in both Regions II and III. One can therefore derive asymptotic forms of the *per-k* kinetic and magnetic stress energy densities, Equations (70), (71), (74) and (75) as given below

$$\lim_{\tilde{k} \rightarrow \infty} \mathcal{R}_{xy} \sim \frac{\eta_T^2 (2\Omega + v_A^2 \eta_H / \eta_T^2) (\gamma_\infty + v_A^2 \eta_P / \eta_T^2)}{v_A^4 + 2v_A^2 (\gamma_\infty \eta_P + 2\Omega \eta_H) + \eta_T^2 (\gamma_\infty^2 + 4\Omega^2)}, \quad (83)$$

$$\lim_{\tilde{k} \rightarrow \infty} \mathcal{M}_{xy} \sim 0, \quad (84)$$

$$\lim_{\tilde{k} \rightarrow \infty} \mathcal{E}_K \sim \frac{1}{2}, \quad (85)$$

$$\lim_{\tilde{k} \rightarrow \infty} \mathcal{E}_M \sim 0, \quad (86)$$

where $\eta_T^2 = \eta_H^2 + \eta_P^2$ and γ_∞ is the solution to Equation (62) for Region II and Equation (63) for Region III. Using Equations (83) and (85) in Equations (68) and (72), we may then approximate the time dependent xy Reynolds stress tensor and kinetic energy density as

$$R_{xy}(t) \approx 2e^{2\gamma_\infty t} \mathcal{R}_{xy}(\tilde{k} \rightarrow \infty) \sum_n 1^n, \quad (87)$$

$$E_K(t) \approx e^{2\gamma_\infty t} \sum_n 1^n. \quad (88)$$

While the infinite sum in Equations (87) and (88) appear to be a divergent series, it is in fact the Riemann zeta function

$$\zeta(s) = \sum_{n=1}^{\infty} \frac{1}{n^s},$$

with $s = 0$ and possesses a finite sum $\zeta(0) = -1/2$ (Hardy 1956). We shall not endeavour to speculate on the implications of this curious feature since an infinite range of scales

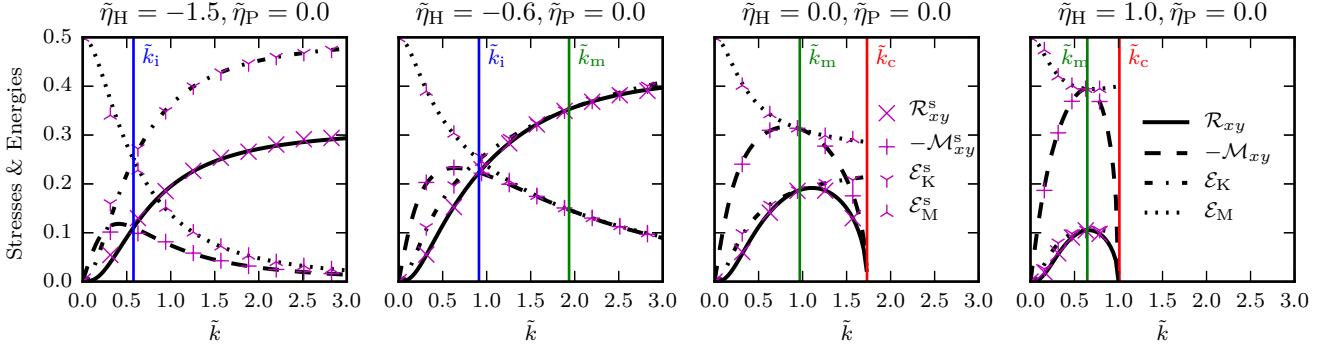


Figure 7. The xy components of the *per-k* Reynolds and Maxwell's stress tensor and the kinetic and magnetic energy densities of the MRI unstable mode, Equations (70), (71), (74) and (75), for different values of the Hall parameter, $\tilde{\eta}_H = -1.5, -0.6, 0.0, 1.0$ and $q = 1.5$ are plotted by the line curves. The discrete markers denote the corresponding values of the said quantities derived from shearing box simulations. Legends with the superscript 's' label the corresponding quantity derived from simulation data.

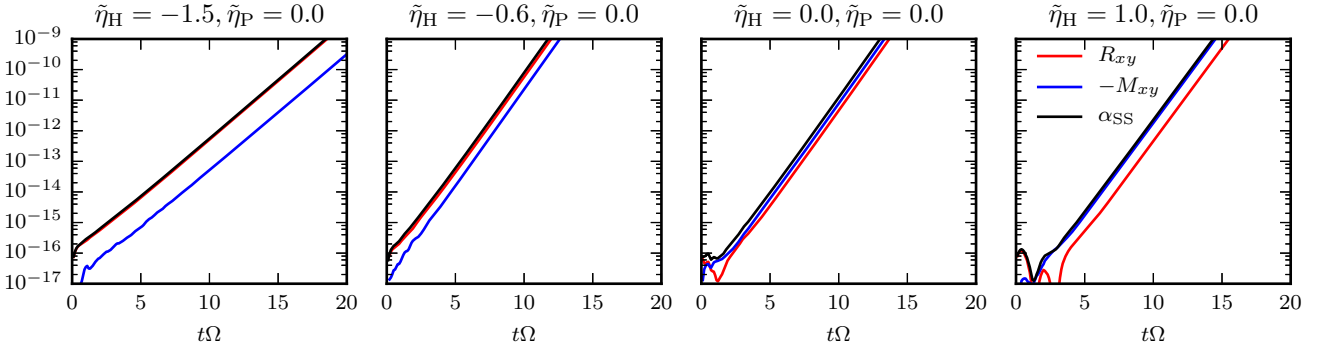


Figure 8. The xy components of the Reynolds stress tensor, Maxwell's stress tensor and the Shakura-Sunyaev α_{SS} parameter of the MRI unstable mode for different values of the Hall parameter, $\tilde{\eta}_H = -1.5, -0.6, 0.0, 1.0$ and $q = 1.5$ obtained from shearing box simulations with $N_z = 256$. In accordance with the results of the linear theory, we find that the Reynolds stress dominates over the Maxwell's stress when $\tilde{\eta}_H < 0$.

will never come to pass as the fluid approximation inevitably breaks down. The alternative is no less dramatic in that a finite series would have the sum $\sum_{n=1}^N 1^n = N$ where N can be rather large.

We are thus led to expect

$$\lim_{t\Omega \gg 1} \frac{-M_{xy}}{R_{xy}} \ll 1, \quad (89)$$

with the ratio becoming increasingly smaller the greater the unstable range of wavelengths accounted for. In a real astrophysical system such as a protoplanetary disk, dissipation due to ohmic and ambipolar diffusion may be large enough in some parts of the disk to keep the kinetic stress R_{xy} and energy density E_K , bounded, by suppressing the unstable growth at smaller length scales. Therefore, the dominance of kinetic stresses may go unchallenged unless dissipation forces the instability to operate within Region I, see Figure 6. On the other hand, if one can find parts of the disk where the diffusivities fall within Regions II and III, one should expect the Reynolds stress to dominate. Figure 7 shows the

per-k kinetic and magnetic xy stress component and energy densities in the dissipationless limit for different values of the Hall parameter, $\tilde{\eta}_H$.

6. COMPARING ANALYTICAL RESULTS WITH NUMERICAL SIMULATIONS

In this section we present the results of unstratified shearing box simulations with a uniform net vertical field including Hall and diffusion, performed using the grid-based higher order Godunov MHD code ATHENA (Stone et al. 2008). The Hall effect is implemented in Athena using an operator-split technique (Bai 2014) that is similar to the dimensionally split scheme proposed by O'Sullivan & Downes (2006, 2007). We use the HLLD Riemann solver and a CTU unsplit integrator with third order reconstruction. The simulations we performed are identical to the test runs reported in Appendix B of Bai 2014.

We adopt an isothermal equation of state and the initial conditions constitute random velocity perturbations of strength, $\delta u/c_s = 10^{-6}$. The default boundary conditions

are periodic in y and z and shearing periodic in x . Our simulations were performed with a plasma beta, defined as the ratio of thermal to magnetic pressure $\beta = 800$, background angular frequency $\Omega = 1$, equilibrium density $\rho_0 = 1$, isothermal sound speed $c_s = 1$ and dimensionless shear rate $q = 3/2$. The computational domain has an extent of $L_x \times L_y \times L_z = 0.1H \times 0.1H \times 2H$. We work with the default grid resolution $N_x \times N_y \times N_z = 4 \times 4 \times 256$.

In order to directly test and compare against the predictions of analytical theory, we run the code by varying the Hall parameter over the different values, $\tilde{\eta}_H = -1.5, -0.6, 0.0, 1.0$ and $\tilde{\eta}_P = 0.0$.⁵ We also perform one additional simulation with the parameters $\tilde{\eta}_H = -1.5$ and $\tilde{\eta}_P = 1.0$. The simulations were run for up to 20 orbits with orbital advection via Fargo enabled. Such short run times suffice for the task at hand since the aim is to test the agreement between our analytical results and the linear evolution of the simulations. We obtain the perturbations, $\delta u_x, \delta u_y, \delta b_x, \delta b_y$, from the Athena output and compute their Fourier transform at time, $t = 11\Omega^{-1}$. We then combine these variables as given by Equations (70), (71), (74) and (75) to obtain the kinetic and magnetic stress components and energies at a given scale.

We have found the simulation and the theoretical results to be in excellent agreement for as many vertical modes, \tilde{k} , as can be reliably resolved. The output of the shearing box simulation conducted with a vertical grid resolution, $N_z = 256$, is over-plotted against the values of the corresponding stresses and energy densities obtained from linear theory in Figure 7. Figure 8 plots the growth in the xy time dependent Reynolds and Maxwell's stress as well as the Shakura-Sunyaev alpha parameter defined as

$$\alpha_{SS} \equiv \frac{\int (\overline{\rho \delta u_x \delta u_y} - \overline{\delta b_x \delta b_y}) dz}{c_s^2 \int \rho dz}, \quad (90)$$

for the same set of parameters $\tilde{\eta}_H = -1.5, -0.6, 0.0, 1.0$, $\tilde{\eta}_P = 0.0$ and $N_z = 256$ and where the overlines denote horizontal averages. In accordance with the implications that followed from Equations (87) and (88), we find that even for such moderate resolutions, the Reynolds stress noticeably dominates the Maxwell's stress during the linear growth of the instability. For a fixed value of $\tilde{\eta}_H = -1.5$, we compare the kinetic and magnetic stress and energy densities with two different values of $\tilde{\eta}_P = 0.0, 1.0$ in Figure 9. Although a finite value of \tilde{k}_i appears to be present with $\tilde{\eta}_P = 1.0$, $-\mathcal{M}_{xy} \gg \mathcal{R}_{xy}$ at \tilde{k}_m and so Maxwell's stress maintains its hegemony over its kinetic counterpart.

Figure 10 compares the values of the xy component of the $per-k$ Reynolds stress tensor obtained from simulations with

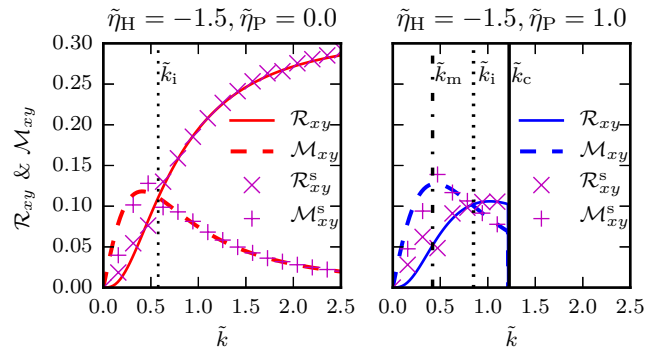


Figure 9. The Reynolds and Maxwell's stress component \mathcal{R}_{xy} and \mathcal{M}_{xy} of the MRI unstable mode with $\tilde{\eta}_H = -1.5$ and $q = 1.5$ without dissipation $\tilde{\eta}_P = 0$ (left panel) and with dissipation $\tilde{\eta}_P = 1.0$ (right panel). The discrete markers denote the corresponding values of the stresses derived from shearing box simulations. Legends with the superscript 's' label the corresponding quantity derived from simulation data.

three different vertical grid resolutions. It is quite apparent that with increasing resolution, the agreement between theory and simulation improves substantially as many more smaller scale modes are reliably resolved. This places a stringent requirement upon the resolution demands while performing simulations of a weakly magnetized shearing system when Hall diffusion is present and dissipation is comparatively weak, if one is to obtain accurate results in accordance with theoretical expectations. In the simulations conducted by Sano & Stone (2002b), the vertical resolution was generally low ($N_z = 32, L_z = H$). However, one can already see in their results that the volume averaged Reynolds and Maxwell's stresses at saturation were the same order of magnitude when $\tilde{\eta}_H < 0$ and $\tilde{\eta}_P < 1$. This is not so for comparable simulations performed with resistivity but without Hall diffusion (Sano et al. 2004) where the xy Maxwell's stress at saturation was larger than the corresponding Reynolds stress. While we have not explored the non-linear regime in our work, we anticipate that with higher grid resolution, one might find stronger mean Reynolds stress perpetuating even at late times. This could be confirmed with dedicated numerical studies.

7. SUMMARY AND DISCUSSION

In this paper, we have carried out a detailed examination of the linear eigenmodes in the shearing sheet framework for a weakly magnetized system subject to non-ideal effects with special focus on Hall diffusion. Although our analysis invoked simplifying assumptions, we have nonetheless been able to go a step further from similar analysis performed in the past and glean certain key attributes governing these modes. A careful examination of the eigenvectors has enabled us to provide a detailed description of the polarization

⁵ Note that the dimensionless Hall parameter in Athena, Q_H , is related to the Hall parameter in our work as $Q_H = \sqrt{2/\beta} \tilde{\eta}_H$.

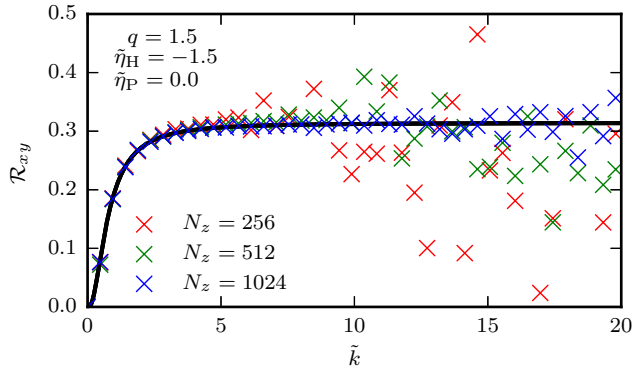


Figure 10. The *per-k* Reynolds stress component \mathcal{R}_{xy} of the MRI unstable mode with $\tilde{\eta}_H = -1.5$ and $q = 1.5$. The crosses denote the corresponding values of the *per-k* stress component derived from shearing box simulations with three different vertical grid resolutions, $N_z = 256, 512, 1024$. The agreement between analytical and numerical results improves at higher wavenumbers as the resolution increases.

properties and to sketch a visual representation of the eigenmodes as they evolves in space and time. By employing the formalism of Pessah et al. (2006), we have also derived expressions for the kinetic and magnetic stresses and energy densities in terms of the complex eigenvector components. This has enabled us to generalize the ratio of the magnetic to kinetic stresses applicable to the later stages of linear evolution of the MRI when subject to Hall diffusion. Our central result is the identification of regimes in the parameter space defined by $(\tilde{\eta}_H, \tilde{\eta}_P)$ wherein the kinetic stresses and energies are found to dominate their magnetic equivalents. This property is in sharp contrast to what one expects of the ideal MRI or the MRI subject to dissipative effects alone.

Since the non-ideal MRI unstable eigenmodes studied here are also exact non-linear solutions of the shearing sheet equations (Kunz & Lesur 2013; Goodman & Xu 1994), the unique traits associated with these modes may carry through or influence the subsequent non-linear evolution of the system. In ideal as well as dissipative MHD (Pessah & Goodman 2009; Latter et al. 2009; Pessah 2010), these so-called channel modes have been shown to be unstable to parasitic instabilities which may result in their ultimate saturation. Kunz & Lesur (2013) is the only work we are aware of that has explored the stability of the Hall-MRI modes to parasitic instabilities. In light of the findings presented here, it would be worthwhile to revisit the question of saturation via parasitic modes, particularly for the case with negative Hall diffusivities ($\tilde{\eta}_H < 0$) and weak dissipation.

There have been a number of recent numerical studies of a weakly magnetized system subject to Hall diffusion (Kunz & Lesur 2013; Lesur et al. 2014; Bai 2014, 2015; Simon et al. 2015) in the shearing box framework. To our knowledge, none of these studies have reported anything resembling the behavior of stresses with $\tilde{\eta}_H < 0$, that we have presented in this paper. We surmise that this may be due to the insufficient vertical grid resolution and comparably strong ohmic and ambipolar diffusion present in virtually all of these simulations. Most of these studies have been performed with primary applications to protoplanetary disks and amongst them, simulations exploring the system with anti-parallel angular momentum and magnetic field vectors have been comparatively few. Simon et al. (2015) did however report the appearance of transient turbulent bursts in their shearing box simulations with all non-ideal effects and anti-parallel angular momentum and magnetic field vectors. However, they attribute this behavior to a non-axisymmetric version of the Hall-Shear instability (Rüdiger & Kitchatinov 2005; Kunz 2008).

Conventional wisdom dictates that the ensuing turbulence in a magnetorotationally unstable system is one that is dominated by magnetic stresses and energies. Astrophysical disks such as those around young stellar objects are thought to harbor regions within them where Hall diffusion is the dominant non-ideal effect (Balbus & Terquem 2001; Kunz & Balbus 2004; Wardle 2007; Wardle & Salmeron 2012; Bai 2011; Xu & Bai 2016). These regions may also be subject to diffusion by ohmic and ambipolar diffusion to varying extents. If the dissipative effects are sufficiently strong, they can act to cut down the range of scales unstable to the MRI and thereby curtail the dominance of kinetic stresses if $\tilde{\eta}_H < 0$. However, there is no definitive estimate at the moment of how prevalent the different non-ideal effects are and to what degree. Therefore, it is still too early to judge whether factors that favor the conditions leading to predominant kinetic stresses may or may not be found. The implications that this role-reversal might have upon the ensuing turbulence warrants further study.

We are grateful to the referee whose comments led to an improved version of the paper. We acknowledge useful discussions with Tobias Heinemann, Oliver Gressel and Leonardo Krapp. We are grateful to Thomas Berlok for help with the simulations and for useful comments on the manuscript. The research leading to these results has received funding from the European Research Council under the European Unions Seventh Framework Programme (FP/2007-2013) under ERC grant agreement 306614.

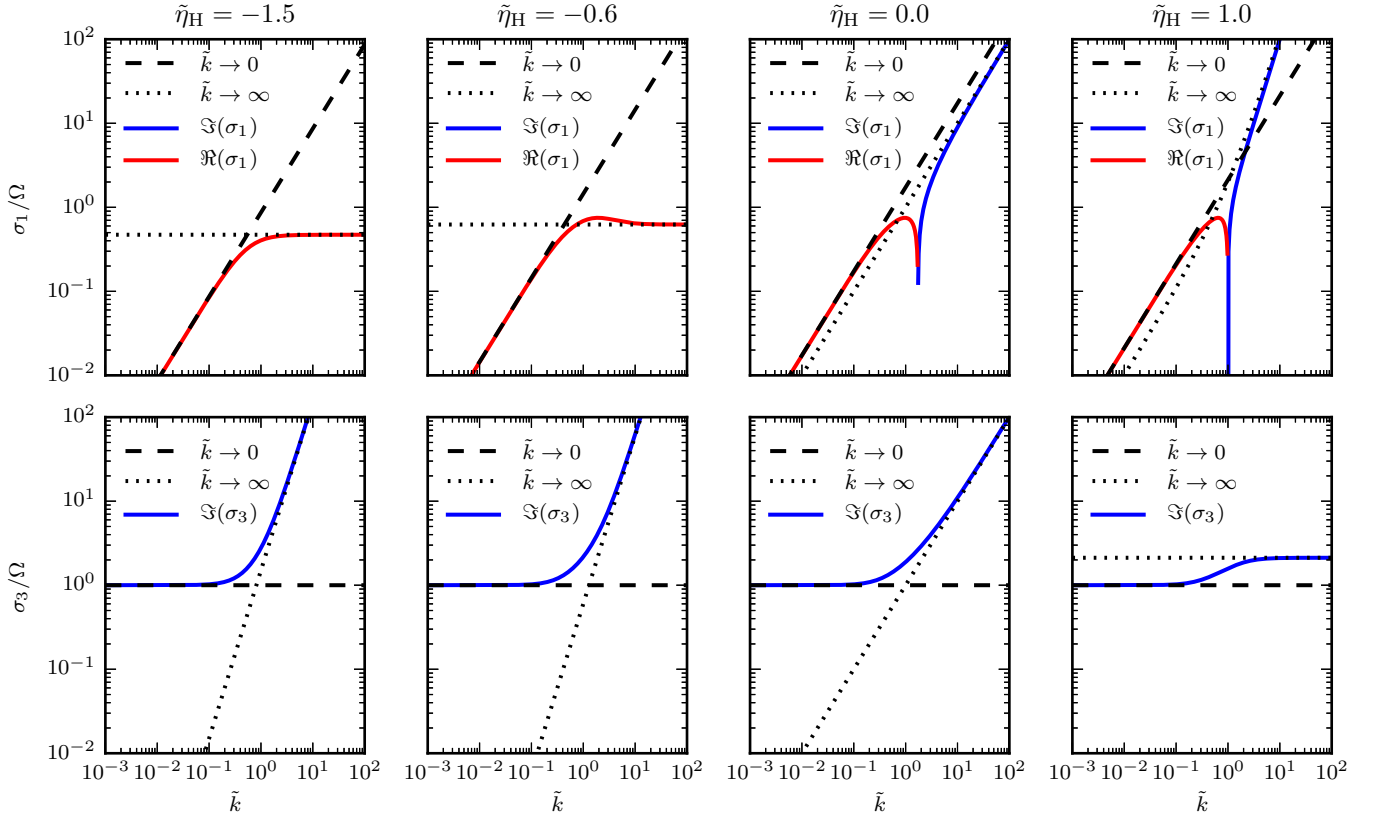


Figure 11. The positive branch solutions, σ_1 and σ_3 , of the eigenvalue problem for four representative values of the Hall parameter, $\tilde{\eta}_H = -1.5, -0.6, 0.0, 1.0$ and $q = 1.5$ in the dissipationless limit. Solid lines represent the numerically computed eigenvalues (the real part in red and the imaginary part in blue). Asymptotic approximations in the low wavenumber limit ($\lim \tilde{k} \rightarrow 0$) and the high wavenumber limit ($\lim \tilde{k} \rightarrow \infty$) are represented by the dashed and dotted lines respectively.

APPENDIX

A. CLASSIFICATION OF THE EIGENMODES IN THE DISSIPATIONLESS LIMIT

Here, we solve the dispersion relation Equation (26) in the dissipationless limit $\omega_\nu = \omega_P = 0$ and describe the nature of the different solutions in some detail. In the limit $M \rightarrow 0$ and choosing the root such that $y = -L/2$ in Equation (35), we find that the roots of Equation (29) given by Equation (37) reduces to

$$\lim_{M \rightarrow 0} \sigma = \pm \sqrt{-\Lambda_0 \mp \sqrt{\Delta_0}}, \quad (\text{A1})$$

where

$$\Lambda_0 = \frac{L_0}{2} \quad \text{and} \quad \Delta_0 = \frac{L_0^2}{4} - N_0, \quad (\text{A2})$$

and

$$\Lambda_0 = \omega_A^2 + \frac{\kappa^2}{2} + \frac{\kappa_H^2}{2}, \quad (\text{A3})$$

$$\Delta_0 = \left(\Omega - \frac{\omega_H}{2}\right)^2 \left[\left(\omega_H + \frac{\kappa^2}{2\Omega}\right)^2 + 4\omega_A^2 \right]. \quad (\text{A4})$$

Setting $\omega_H \rightarrow 0$ in Equations (A3) and (A4), we recover the ideal MRI solutions (Pessah et al. 2006). For the purpose of identification, we shall designate the four eigenvalues as

$$\sigma_1 = \gamma, \quad \sigma_2 = -\gamma, \quad \sigma_3 = i\omega, \quad \sigma_4 = -i\omega, \quad (\text{A5})$$

where

$$\gamma = \sqrt{-\Lambda_0 + \sqrt{\Delta_0}} \quad \text{and} \quad \omega = \sqrt{\Lambda_0 + \sqrt{\Delta_0}}. \quad (\text{A6})$$

The notation γ and ω has been chosen to be redolent of the unstable and oscillatory nature of the corresponding eigenmodes. The positive branch eigensolutions, σ_1 and σ_3 , have the following asymptotic forms, at very low and high wavenumbers

$$\lim_{\tilde{k} \rightarrow 0} \sigma \sim \begin{cases} \omega_A \sqrt{q(2-q)^{-1} + q\tilde{\eta}_H} \text{ R.E.P if } \tilde{\eta}_H \geq 0 \text{ and L.E.P if } \tilde{\eta}_H < 0, \\ i\kappa, \quad \text{L.E.P} \end{cases} \quad (\text{A7})$$

$$\lim_{\tilde{k} \rightarrow \infty} \sigma \sim \begin{cases} i\omega_H, \quad \text{R.E.P if } \tilde{\eta}_H \geq 0 \text{ and L.E.P if } \tilde{\eta}_H < 0, \\ i\omega_G, \quad \text{L.E.P} \end{cases} \quad (\text{A8})$$

where ω_G is the so-called gyration frequency (Heinemann & Quataert 2014)

$$\omega_G = \sqrt{\left[2\Omega + \frac{\omega_A^2}{\omega_H}\right] \left[(2-q)\Omega + \frac{\omega_A^2}{\omega_H}\right]}. \quad (\text{A9})$$

In the absence of rotation and shear, ω_G corresponds to the ion-cyclotron frequency, $\omega_{ci} = eB/m_i c$ reduced by the ionization fraction n_e/n . The acronyms R.E.P and L.E.P stand for Right and Left Elliptically Polarized respectively and indicates the direction of polarization of the oscillatory eigenmodes as seen by an observer looking down perched above the disk midplane.

The Coriolis force and the Hall effect endow the oscillatory modes with a circular polarization or helicity. The effect of shear is to make the polarization elliptical. Hall diffusion has the added effect of bringing about divergent behavior of the oscillatory modes at large wavenumbers. One of the otherwise Alfvénic branches breaks out into what is commonly referred to as the Whistler mode where the frequency varies quadratically with wavenumber. The other Alfvén branch asymptotes to a maximum frequency corresponding to the reduced ion-cyclotron frequency as the wavelength grows smaller.

Under ideal MHD conditions, an infinitesimal perturbation executes a circular trajectory due to the Coriolis force. The shear eccentrically stretches this motion towards positive azimuth inwards from the point of origin and towards negative azimuth outwards. The Lorentz tension is activated and tries to restore the fluid element thereby transferring angular momentum from the inward moving fluid element to the tethered element moving outwards. The respective fluid elements fall further inwards and outwards to compensate and the egression is greater at intermediate lengthscales where tension is weakest. This is the standard physical picture of the MRI (Balbus & Hawley 1998). When $\tilde{\eta}_H > 0$, the Hall effect introduces an “epicyclic motion” of its own (Balbus & Terquem 2001) that has the opposite sense of the Coriolis induced epicycles. At smaller length scales, this push-back is intensified and together with tension, suppresses any unstable motion. When $\tilde{\eta}_H < 0$, the Hall effect induced epicycles have the same sense as the Coriolis motion and moreover acts to negate the restoring magnetic tension forces at the smaller lengthscales. These epicycles respond at the frequency ω_G which is also now purely imaginary and leads to continued exponential growth at ever smaller lengthscales. Wardle & Salmeron (2012) refer to the instability as operating in the “cyclotron limit” at the high wavenumber end.

Figure 11 shows the positive eigensolutions, σ_1 and σ_3 as a function of wavenumber for four representative values of $\tilde{\eta}_H$. The asymptotic forms given by Equations (A7) and (A8) are plotted over the exact solutions for comparison. Notice the eigensolutions σ_1 and σ_3 , splitting into separate branches with $\tilde{\eta}_H = 1$ in Figure 11, at high wavenumbers. For the sake of identification, we shall refer to modes that asymptote to the frequency ω_G , as simply the cyclotron mode. Bear in mind however that when $-1/2 < \tilde{\eta}_H < \infty$, σ_1 becomes oscillatory beyond the cut-off wavenumber \tilde{k}_c . The change in sign of $\tilde{\eta}_H$ effects an interchange of the Whistler and cyclotron behavior on the modes, σ_1 and σ_3 , at high wavenumbers. Furthermore when $-2 < \tilde{\eta}_H < -1/2$, ω_G is purely imaginary and corresponds to the large wavenumber growth rate of the unstable mode, σ_1 .

REFERENCES

- Armitage, P. J. 2011, *ARA&A*, 49, 195
- Bai, X.-N. 2011, *ApJ*, 739, 51
- Bai, X.-N. 2014, *The Astrophysical Journal*, 791, 137.
- , 2015, *The Astrophysical Journal*, 798, 84.
- <http://adsabs.harvard.edu/abs/2015ApJ...798...84B>
- Balbus, S. A., & Hawley, J. F. 1998, *Reviews of Modern Physics*, 70, 1
- <http://adsabs.harvard.edu/abs/2014ApJ...791..137B>

- Balbus, S. A., & Terquem, C. 2001, *The Astrophysical Journal*, 552, 235.
<http://adsabs.harvard.edu/abs/2001ApJ...552..235B>
- Bejarano, C., Gómez, D. O., & Brandenburg, A. 2011, *The Astrophysical Journal*, 737, 62.
<http://adsabs.harvard.edu/abs/2011ApJ...737...62B>
- Béthune, W., Lesur, G., & Ferreira, J. 2016, *Astronomy & Astrophysics*, 589, A87.
<http://www.aanda.org/10.1051/0004-6361/201527874>
- Goldreich, P., & Lynden-Bell, D. 1965, *MNRAS*, 130, 125
- Goodman, J., & Xu, G. 1994, *ApJ*, 432, 213
- Hardy, G. 1956, *Divergent series*, Oxford: Clarendon.
<http://opac.inria.fr/record=b1109376>
- Heinemann, T., & Quataert, E. 2014, *ApJ*, 792, 70
- Kunz, M. W. 2008, *Monthly Notices of the Royal Astronomical Society*, 385, 1494.
<http://adsabs.harvard.edu/abs/2008MNRAS...385.1494K>
- Kunz, M. W., & Balbus, S. A. 2004, *MNRAS*, 348, 355
- Kunz, M. W., & Lesur, G. 2013, *Monthly Notices of the Royal Astronomical Society*, 434, 2295.
<http://adsabs.harvard.edu/abs/2013MNRAS...434.2295K>
- Latter, H. N., Lesaffre, P., & Balbus, S. A. 2009, *MNRAS*, 394, 715
- Lesur, G., Kunz, M. W., & Fromang, S. 2014, *Astronomy and Astrophysics*, 566, A56.
<http://adsabs.harvard.edu/abs/2014A%26A...566A..56L>
- O'Sullivan, S., & Downes, T. P. 2006, *MNRAS*, 366, 1329
- . 2007, *MNRAS*, 376, 1648
- Pandey, B. P., & Wardle, M. 2008, *Monthly Notices of the Royal Astronomical Society*, 385, 2269.
<http://mnras.oxfordjournals.org/cgi/doi/10.1111/j.1365-2966.2008.12998.x>
- Pessah, M. E. 2010, *ApJ*, 716, 1012
- Pessah, M. E., & Chan, C.-k. 2008, *The Astrophysical Journal*, 684, 498.
<http://adsabs.harvard.edu/abs/2008ApJ...684..498P>
- Pessah, M. E., Chan, C.-K., & Psaltis, D. 2006, *MNRAS*, 372, 183
- Pessah, M. E., & Goodman, J. 2009, *ApJL*, 698, L72
- Rüdiger, G., & Kitchatinov, L. L. 2005, *Astronomy and Astrophysics*, 434, 629.
<http://adsabs.harvard.edu/abs/2005A%26A...434..629R>
- Sano, T., Inutsuka, S.-i., Turner, N. J., & Stone, J. M. 2004, *ApJ*, 605, 321
- Sano, T., & Stone, J. M. 2002a, *The Astrophysical Journal*, 570, 314.
<http://adsabs.harvard.edu/abs/2002ApJ...570..314S>
- . 2002b, *The Astrophysical Journal*, 577, 534.
<http://adsabs.harvard.edu/abs/2002ApJ...577..534S>
- Simon, J. B., Lesur, G., Kunz, M. W., & Armitage, P. J. 2015, arXiv:1508.00904 [astro-ph], arXiv: 1508.00904.
<http://arxiv.org/abs/1508.00904>
- Stone, J. M., Gardiner, T. A., Teuben, P., Hawley, J. F., & Simon, J. B. 2008, *ApJS*, 178, 137
- Turner, N. J., Fromang, S., Gammie, C., et al. 2014, *Protostars and Planets VI*, 411
- Wardle, M. 1999, *Monthly Notices of the Royal Astronomical Society*, 307, 849.
<http://adsabs.harvard.edu/abs/1999MNRAS...307..849W>
- Wardle, M. 2007, *Ap&SS*, 311, 35
- Wardle, M., & Salmeron, R. 2012, *Monthly Notices of the Royal Astronomical Society*, 422, 2737.
<http://adsabs.harvard.edu/abs/2012MNRAS...422.2737W>
- Xu, R., & Bai, X.-N. 2016, *ApJ*, 819, 68